applied sciences

MDPI

Article

Efficient Adsorptive Removal of Methyl Orange from Aqueous Solutions Using a Cu_2O/CuO Nanocomposite

Yordani Arce-Argote *, Antonella Soncco, Rodrigo Rios-Cabala, Albeniz Huaracallo, Marcelo Rodriguez and Rivalino Guzmán

Professional School of Materials Engineering, Academic Department of Materials Engineering, Faculty of Process Engineering, Engineering Campus, Universidad Nacional de San Agustin de Arequipa (UNSA), Av. Independencia s/n, Arequipa 04001, Peru; asonccohu@unsa.edu.pe (A.S.); rriosc@unsa.edu.pe (R.R.-C.); ahuaracalloi@unsa.edu.pe (A.H.); mrodriguezv@unsa.edu.pe (M.R.); rguzmana@unsa.edu.pe (R.G.)

* Correspondence: yarcea@unsa.edu.pe; Tel.: +51-975812688

Abstract

The persistence of azo dyes in industrial effluents poses significant environmental risks; therefore, there is a need to develop effective adsorbents. This study investigates the efficiency of a Cu_2O/CuO nanocomposite as an adsorbent for the removal of a model dye, methyl orange (MO), from aqueous solutions. The material was characterized by XRD, SEM and BET analyses, revealing a dominant Cu_2O phase (96 wt%) with CuO fractions, and an average particle size of ~18 nm paired with a specific surface area of 19.54 m^2 g^{-1}. FTIR and TOC assays revealed the adsorption and degradation of MO by action of the nanocomposite. Operational parameters such as adsorbent dosage, initial dye concentration, pH, and the point of zero charge (PZC) were investigated. Under the optimized conditions, the nanocomposite achieved a dye removal efficiency of 97.0%. The kinetic results showed a strong correlation with the pseudo-second-order model. Furthermore, isotherm analysis revealed that the adsorption process is best described by the Langmuir–Freundlich model, demonstrating an outstanding maximum theoretical adsorption capacity (q_{max}) of 254.76 mg g^{-1}, which closely aligns with the experimental value (249.48 mg g^{-1}). The findings demonstrated that the synthesized Cu_2O/CuO nanocomposite acts as an efficient and promising adsorbent for the remediation of dye-contaminated waters.

Keywords: nanocomposite; Cu_2O/CuO; adsorption; methyl orange; kinetics; isotherm

1. Introduction

The textile industry represents one of the sectors with the largest water footprint globally and is characterized by an intensive demand for water for its finishing and dyeing processes [1]. As a massive consumer of synthetic dyes, this sector generates residual aqueous effluents that disrupt the balance of aquatic ecosystems and pose a threat to human health due to their potential toxic, carcinogenic, and mutagenic effects [2,3]. Among the products used during the textile process are synthetic dyes, mainly azo-type dyes, which account for more than half of global production. Methyl orange (MO) is widely used as a model pollutant to evaluate the efficiency of adsorption and photocatalysis processes [2,4].

For the remediation of effluents contaminated with MO, various technologies have been implemented, such as electrochemical oxidation [5], photocatalytic oxidation [6], membrane separation [7], coagulation/flocculation [8], microbiological treatment [9] and advanced oxidative processes [10]. However, scaling these systems for industrial application presents significant economic and operational challenges. Biological treatments

Check for updates

Academic Editor: María Ángeles Martín-Lara

Received: 4 February 2026
Revised: 7 April 2026
Accepted: 8 April 2026
Published: 10 April 2026

Copyright: © 2026 by the authors. Licensee MDPI, Basel, Switzerland. This article is an open access article distributed under the terms and conditions of the Creative Commons Attribution (CC BY) license.

are frequently ineffective due to the recalcitrant and highly stable nature of synthetic azo dyes [11]. Membrane filtration suffers from high energy consumption and severe membrane fouling, while AOPs require expensive chemical reagents, complex infrastructure, and extensive energy inputs [12,13]. Adsorption, on the other hand, is widely recognized as one of the most promising and scalable technologies due to its operational simplicity, low initial capital cost, and high efficiency, even at low pollutant concentrations [12,14]. In contrast, adsorption processes offer more advantages than traditional technologies due to their simplicity of design, low cost, and high efficiency [2]. This process consists of the fixation of contaminant species onto the active sites of the solid adsorbent through physical (physisorption) or chemical (chemisorption) interactions [2,15]. By utilizing straightforward synthesis routes to create high-capacity nanomaterials, the required adsorbent dosage and associated operational costs can be significantly minimized, making it a highly competitive alternative for industrial textile wastewater treatment.

Various adsorbents such as biochar [16], clays [17], inorganic metal oxides [18–21], and zeolites [22] have been studied for the removal of MO. However, despite their application, these methods face practical barriers such as limited adsorption capacities, high manufacturing costs, and multi-step synthesis processes. Therefore, a complementary alternative to this method is nanotechnology, which offers materials with large specific surface areas and high removal capacities (close to 90%), among which, nanoscale semiconductor metal oxides stand out [3,4,15]. Unlike pure metallic nanoparticles, these oxides exhibit greater physicochemical stability, thermal resistance, and workability over a wide pH range [3]. In particular, copper oxides (CuO and Cu_2O) have demonstrated exceptional potential due to their dual behavior. These semiconductor nanomaterials operate effectively both under dark conditions, governed by physical and chemical adsorption mechanisms, and under low light exposure, where synergy between adsorption and photocatalytic activity occurs [23]. Therefore, the Cu_2O/CuO nanoparticle pair is projected to be a promising candidate for experimental adsorption practices under dark conditions (pure adsorption) and under light conditions (combined processes), especially for the removal of contaminants in aquatic systems and application at the industrial scale.

This study presents a facile approach to synthesize a Cu_2O/CuO nanocomposite and systematically evaluate its adsorptive behavior toward methyl orange in aqueous solution under dark conditions using UV–Vis spectroscopy and Total Organic Carbon assays. Operational parameters such as pH and contact time were optimized to maximize removal efficiency, while the methyl orange concentration range and initial low adsorbent dosage were specifically designed to force the system to saturation, allowing for the accurate evaluation of the material's maximum adsorption capacity.

2. Materials and Methods

2.1. Materials

Copper (II) sulfate pentahydrate ($CuSO_4 \cdot 5H_2O$, 99.0%), L-ascorbic acid ($C_6H_8O_6$, 99.0%) and polyvinylpyrrolidone (K10, M.W. ~10,000 g mol^{-1}) were purchased from Oxford Lab Fine Chem LLP (Palghar, India). EMSURE® sodium hydroxide (NaOH) was acquired from Merck KGaA (Darmstadt, Germany). The anionic dye methyl orange ($C_{14}H_{14}N_3NaO_3S$, 327.34 g mol^{-1}), used as a model contaminant, was purchased from Merck KGaA (Darmstadt, Germany). All chemicals used were of analytical grade and were employed without further purification. Type I Milli-Q® (Millipore, Molsheim, France) water (18.2 MΩ cm) was used for the preparation of all aqueous solutions and synthesis processes.

2.2. Synthesis Process

The Cu_2O/CuO nanocomposite was synthesized by a liquid-phase chemical precipitation method (Figure 1). First, 0.5 g of $CuSO_4 \cdot 5H_2O$ was dissolved in 40 mL of ultrapure water under constant magnetic stirring (300 rpm) at room temperature. Following this, 40 mL of a 0.1 mmol L^{-1} polyvinylpyrrolidone (PVP) solution was added as a stabilizing agent while maintaining stirring to ensure homogeneous dispersion of the metal precursor. Next, 40 mL of NaOH (0.2 mol L^{-1}) and 40 mL of AA (0.15 mol L^{-1}), used as a reducing agent, were simultaneously added dropwise. After completing the addition, the reaction mixture was kept under continuous stirring for 15 min to promote nucleation and controlled growth of the nanoparticles. The resulting precipitate was recovered by centrifugation and washed three times with ultrapure water to remove unreacted reagents and soluble impurities. Finally, the solid was dried in an oven at 50 °C overnight and stored for subsequent characterization and adsorptive evaluation.

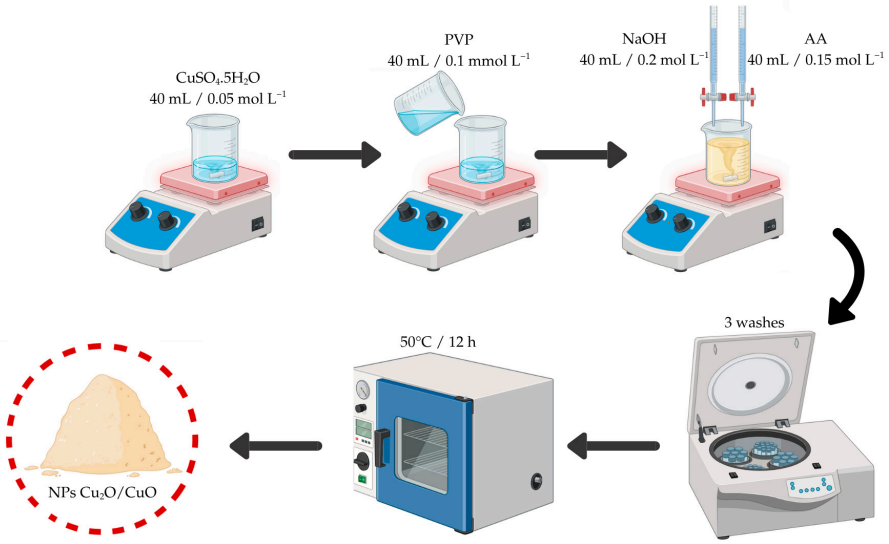

Figure 1. Experimental flowchart of the synthesis of the Cu_2O/CuO nanocomposite.

2.3. Characterization Techniques

To determine the phase, crystallinity, and purity of the nanoparticles, X-ray diffraction (XRD) analyses were performed using a Rigaku SmartLab SE diffractometer (Akishima-shi, Tokyo, Japan) with Cu–Kα radiation (λ = 1.5406 Å), operated at 40 kV and 45 mA over a 2θ angular range of 25° to 80°. The average crystallite size was calculated using the Debye–Scherrer equation with X'Pert HighScore Plus (version 3.0e) software. The morphology and size of the nanoparticles were analyzed by FIB-SEM using a Thermo Fisher Scios 2 DualBeam instrument (ThermoFisher Scientific, Waltham, MA, USA). equipped with an EDS detector for semi-quantitative elemental analysis. The specific surface area was determined using the Brunauer–Emmett–Teller (BET) method using a Gemini VII 2390T instrument (Micromeritics Instrument Corp., Norcross, GA, USA) at 300 mmHg min^{-1} with 11 points from 0.05 to 0.30 P/P_0 in relative pressure, using N_2 at 77.3 K. The absorbance spectrum of methyl orange was recorded over the wavelength range of 200 to 800 nm using a Lambda 365+ UV–Vis spectrophotometer (PerkinElmer, Hopkinton, MA, USA). Fourier transform infrared (FTIR) analysis was conducted using a Bruker Invenio R spectrometer (Bruker Optik GmbH, Ettlingen, Germany). Total Organic Carbon content for MO removal was determined using a Thermalox TOC-TN analyzer (Sercon Instruments, Crewe, UK).

2.4. Batch Adsorption Tests for MO Removal

Adsorption experiments were carried out in a batch system to evaluate the capacity of the Cu_2O/CuO nanocomposite for the removal of the anionic dye methyl orange (MO). To determine the optimal process conditions and assess the effect of operational variables, the one-factor-at-a-time method was employed, evaluating the following experimental parameters: initial dye concentration (10, 20, 40, 60, 80 and 100 mg L^{-1}), nanoparticle dosage (0.1, 0.2, 0.4, 0.6, 0.8, 1, 1.2, 1.4 and 1.6 mg mL^{-1}), and solution pH (6, 9, 10, and 11). The volume of the MO solution was kept constant at 50 mL throughout the experimental runs. The adsorption process was conducted in the dark under constant stirring for 180 min, with 4 mL aliquots withdrawn every 30 min. Next, the suspension was centrifuged at 6000 rpm for 5 min to separate the nanoparticles from the aqueous medium. The residual MO concentration was determined by UV–Vis spectroscopy at a wavelength of 464 nm. Prior to this, a calibration curve was constructed using standard MO solutions, obtaining a linear correlation coefficient of $R^2 = 0.9998$. All adsorption experiments were conducted in triplicate, and the relative standard deviation was found to be less than 3%.

The removal efficiency at a given time was calculated using Equation (1), while the amount of MO adsorbed per unit mass (*qe*) was determined using Equation (2).

$$\% \, removal = \frac{C_0 - C_t}{C_0} * 100 \quad (1)$$

$$q_e = (C_0 - C_e)\frac{V}{m} \quad (2)$$

where C_e (mg L^{-1}) indicates the equilibrium concentration; C_0 and C_t (mg L^{-1}) represent the initial MO concentration and the concentration at time *t* (min), respectively; *qe* (mg g^{-1}) denotes the amount of dye adsorbed per unit mass of the Cu_2O/CuO nanocomposite; *V* (L) is the solution volume; and *m* (g) corresponds to the mass of the Cu_2O/CuO nanocomposite.

2.5. Determination of the Point of Zero Charge (PZC)

The point of zero charge (PZC), defined as the pH at which the surface of the material is electrically neutral, was determined using the pH drift method [24]. This parameter is fundamental for predicting the surface charge of the adsorbent during the adsorption process. For the assay, a series of flasks containing 30 mL of a solution of NaCl (0.1 mol L^{-1}), an inert electrolyte, were prepared. The initial pH was then adjusted within the range of 2 to 12 (pH_i) using HCl and NaOH solutions (0.1 mol L^{-1}), as appropriate. Then, 20 mg of the adsorbent were added to each flask; the flasks were sealed and kept under orbital agitation at 250 rpm for 72 h. After the contact time, the final pH (pH_f) was recorded, and Equation (3) was used to graphically estimate the PZC of the material, defined as the pH value at which the material exhibits a net zero surface charge (i.e., $\Delta pH = 0$) [25].

$$\Delta pH = pH_f - pH_i \quad (3)$$

3. Results and Discussion

3.1. Characterization

3.1.1. X-Ray Diffraction

Figure 2 shows that the diffractogram of the Cu_2O/CuO nanocomposite exhibits intense and well-defined diffraction peaks at 2θ angles of 29.6°, 36.4°, 42.3°, 52.5°, 61.4°, 73.5°, and 77.4°, which correspond to the crystallographic planes (110), (111), (200), (211), (220), (311), and (222), respectively. These planes are characteristic of the cubic cuprite (Cu_2O) structure and are consistent with the reference pattern COD 96-900-7498. Although the diffraction profile is dominated by the Cu_2O phase, quantitative analysis by Rietveld

refinement revealed the formation of a heterostructure composed of 96 wt% Cu_2O and 4 wt% tenorite (CuO). The identification of this minor phase is attributed to the fitting of the experimental pattern with the reference patterns of Cu_2O and CuO (COD 96-901-5715), in which the baseline asymmetry between the (111) and (200) planes suggests the contribution of low-intensity reflections characteristic of the (111) and (200) planes of CuO. The formation of this heterostructure is associated with the high chemical stability of CuO, which leads to an enhancement of the photoresponse of the system and protection of Cu_2O against photocorrosion [23]. Finally, the average crystallite size calculated using the Scherrer equation from the most intense (111) peak was 7 nm.

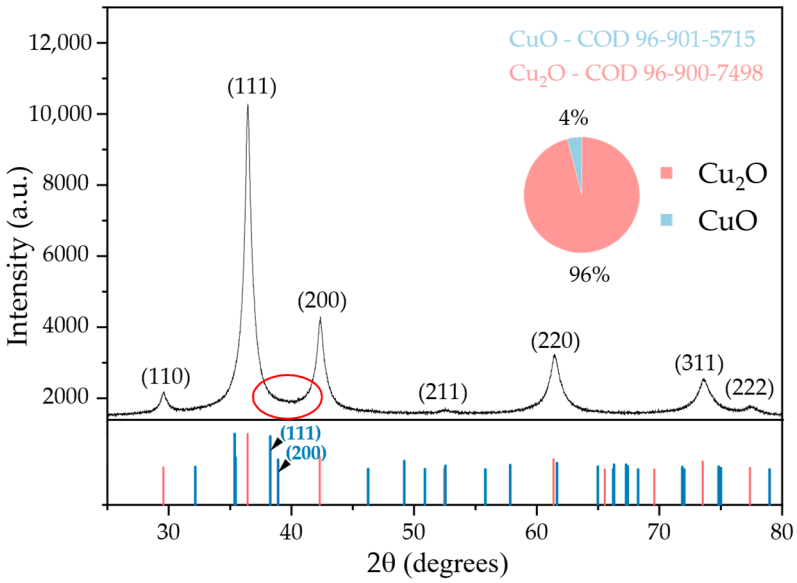

Figure 2. XRD pattern of Cu_2O/CuO nanocomposite.

3.1.2. Scanning Electron Microscopy (SEM)-EDS Analysis

Figure 3a shows SEM micrographs at low and high magnification, revealing the homogeneous morphology of the synthesized material. Figure 3b shows the quasi-spherical shape of the Cu_2O/CuO nanocomposite with remarkable uniformity and dispersion. To determine the nanoparticle size distribution, at least 200 nanoparticles were measured, resulting in an average size of 18 ± 4 nm. The difference observed between this particle size and the crystallite size previously determined by XRD (~7 nm) suggests that the nanoparticles are formed by aggregates of several coherent crystallites.

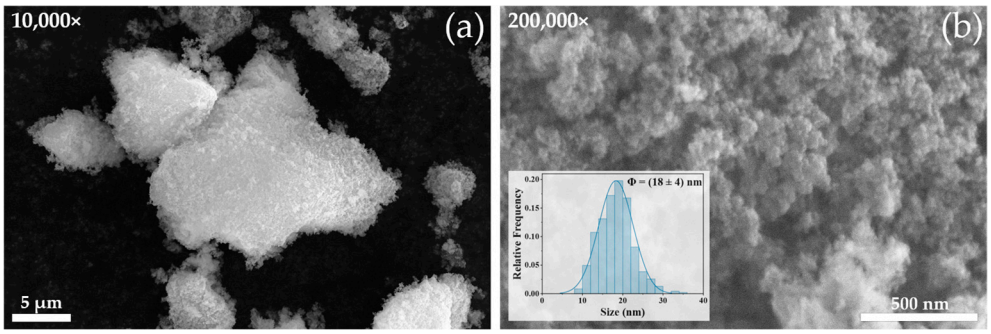

Figure 3. SEM micrographs of the Cu_2O/CuO nanocomposite. (**a**) Low-magnification image (10,000×) showing the general morphology. (**b**) High-magnification image (200,000×) revealing the quasi-spherical shape of the nanoparticles.

Although the nanoparticle size is smaller than that reported in the literature, it is presumed that its use has a superior or comparable effect to that reported in analogous studies evaluating dye adsorption; for example, Liao et al. [26] used 50 nm nanoparticles to remove amaranth, while other authors [27–29] obtained nanoparticles larger than 200 nm for the removal of anionic azo dyes. Regarding elemental composition, the EDS analysis presented in Figure 4 confirmed intensified signals of Cu and O, with no traces of synthesis-derived contaminants such as S, H, and Na. In addition, the approximate atomic ratio of 2:1 corroborates the predominantly Cu_2O stoichiometry.

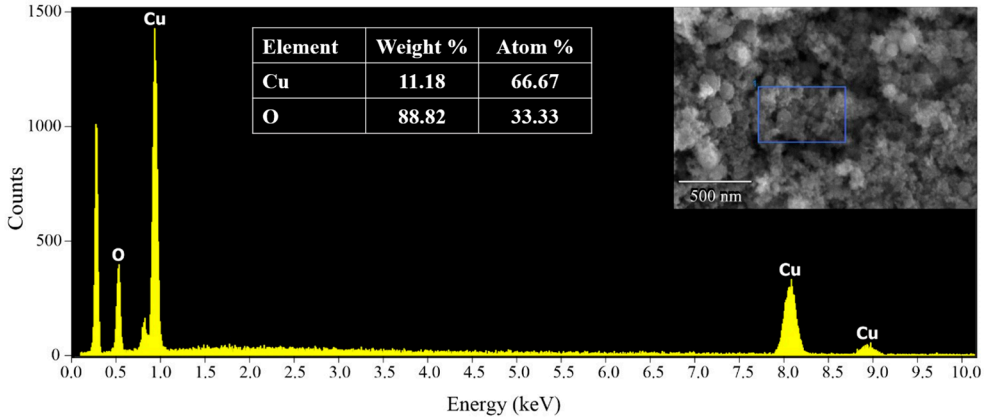

Figure 4. EDS spectrum of the Cu_2O/CuO nanocomposite The inset shows the corresponding SEM image, where the blue square indicates the selected area for the elemental analysis.

3.1.3. Surface and Pore Analysis

The surface properties of the Cu_2O/CuO nanocomposite were determined using N_2 adsorption and desorption isotherms (Figure 5), which show a clear hysteresis loop and a type IV isotherm, indicating the presence of mesopores. The BET surface area was determined to be 19.54 m^2 g^{-1} and the DFT total pore volume was 0.103 cm^3 g^{-1}. The obtained result is close to the 23.3 m^2 g^{-1} surface area reported by Peng et al. [29], who used ultrasound-assisted synthesis, and higher than the 4.5 m^2 g^{-1} obtained using green synthesis [30].

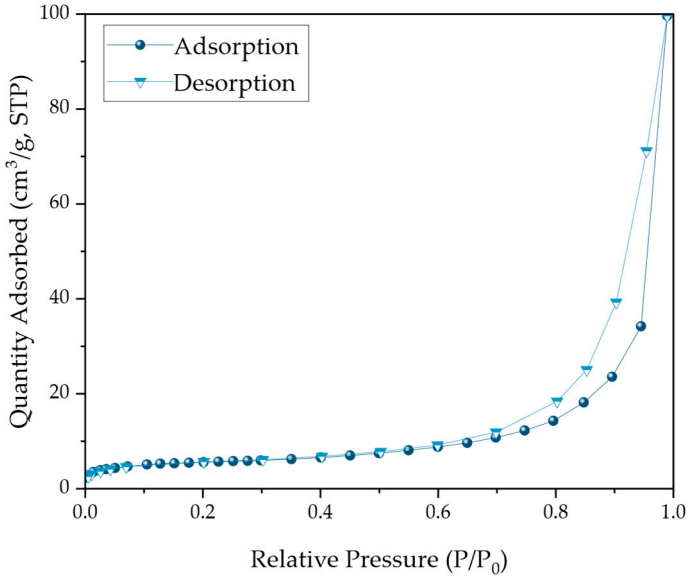

Figure 5. Nitrogen adsorption–desorption BET isotherms of the Cu_2O/CuO nanocomposite.

3.1.4. FTIR Spectroscopy

FTIR spectroscopy was performed (results shown in Figure 6a) and the spectrum of the nanocomposite before adsorption exhibited characteristic metal–oxygen lattice vibrations in the low-frequency region, specifically a strong, broad band around 600 cm^{-1} corresponding to the Cu–O stretching of the Cu_2O/CuO heterostructure [21,30].

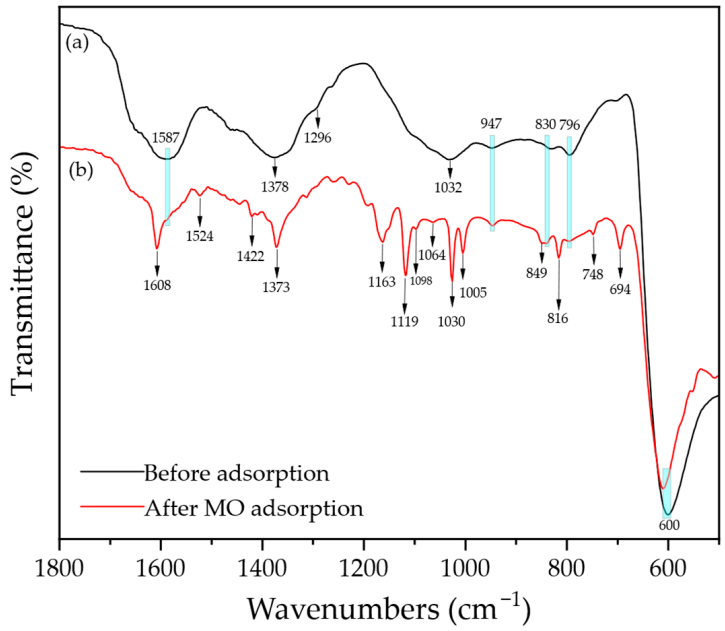

Figure 6. FTIR spectra of the Cu_2O/CuO nanocomposite (**a**) before and (**b**) after methyl orange (MO) adsorption.

Following the adsorption process (Figure 6b), several new characteristic peaks emerged on the spectrum of the nanocomposite. According to the assignments reported by [31], these new signals confirm the presence of MO molecules on the adsorbent surface. Specifically, the peaks at 1422 and 1373 cm^{-1} correspond to the vibrations of the methyl group. The signals at 748, 816 and 849 cm^{-1} result from the C–H bond absorptions of the di-substituted benzene rings. Furthermore, the distinct peaks appearing at 694, 1030, 1064, 1098 and 1119 cm^{-1} are assigned to the vibrations of the sulfonic group ($–SO_3^-$) [31]. A new peak emerged at 1524 cm^{-1}, signifying the N=N stretching of MO [24], while the sharp signals at 1587 and 1608 cm^{-1} are attributed to the C=C stretching vibrations of the aromatic skeleton. Thus, these FTIR results provide evidence for the successful adsorption of MO onto the Cu_2O/CuO nanocomposite.

3.2. Adsorption Performance

Figure 7a illustrates the temporal evolution of the absorbance spectra. A progressive and significant decrease in the intensity of the characteristic absorption peak located at λ_{max} = 464 nm [32] is observed. This reduction occurs continuously from the initial time t = 0 up to 180 min. In Figure 7b, the change in the coloration of the solution is presented, transitioning from an intense orange to being nearly colorless after the treatment. This visually corroborates the removal of the chromophore group of methyl orange from the aqueous phase, confirming the high potential of the Cu_2O/CuO nanocomposite as an adsorbent material [33].

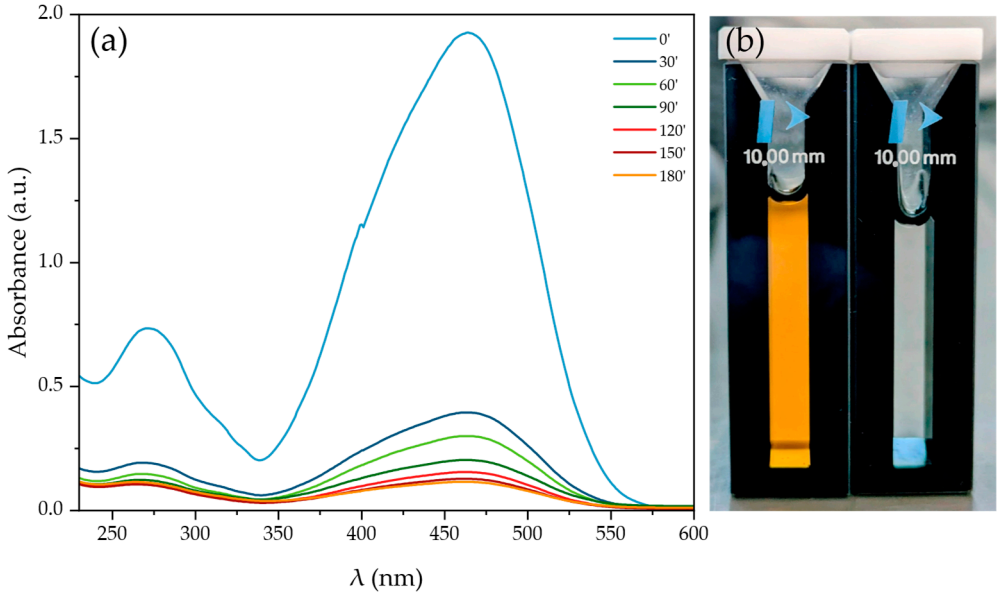

Figure 7. (**a**) Visual comparison of the methyl orange solution before and after the adsorption process; (**b**) Evolution of the UV–Vis absorption spectra of MO as a function of time using the Cu_2O/CuO nanocomposite.

3.2.1. Effect of Initial MO Concentration

Figure 8 illustrates the effect of varying the initial MO concentration (10, 20, 40, 60, 80, and 100 mg L^{-1}) on the adsorption performance, while maintaining a constant adsorbent dosage of 0.2 mg mL^{-1} at pH 6 over a period of 180 min. A dependence between the adsorption behavior and the initial dye concentration was observed as the initial concentration increased from 10 to 100 mg L^{-1}. In contrast, the removal efficiency initially increased from 53.2% to a maximum of 70.2% at 40 mg L^{-1}, before gradually declining to 52.3% at the highest concentration (100 mg L^{-1}). These results indicate that, under the studied conditions, an initial concentration of 40 mg L^{-1} provides the optimal balance for maximum removal efficiency.

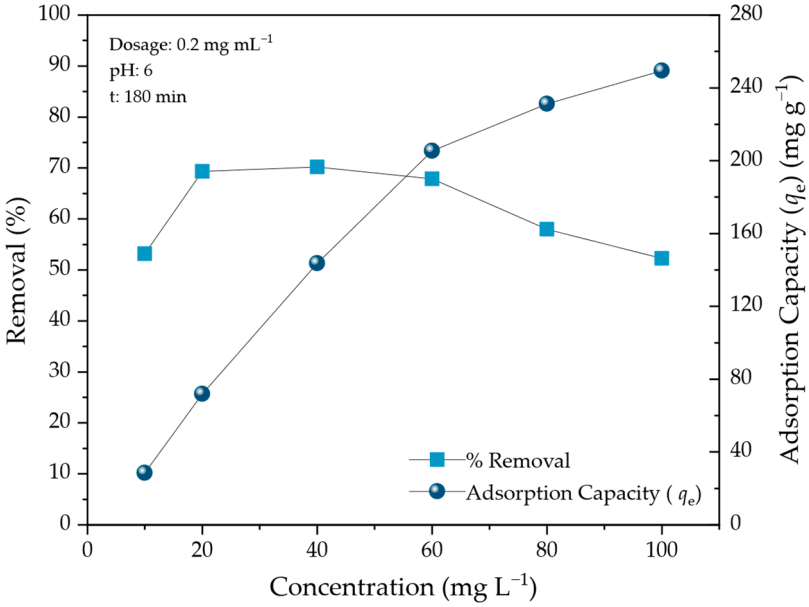

Figure 8. Effect of the initial concentration on the removal efficiency and adsorption capacity (q_e) using Cu_2O/CuO.

The continuous increase in q_e is primarily driven by the higher concentration gradient at the solid–liquid interface [34–36]. This gradient acts as a driving force to overcome the mass transfer resistance of MO molecules between the aqueous and solid phases, facilitating their migration to the nanocomposite surface [27,36]. At lower initial concentrations (10 to 40 mg L^{-1}), the ratio of available active binding sites to dye molecules is high. Thus, increasing the dye concentration raises the collision frequency between anionic MO molecules and the surface of the Cu_2O/CuO NPs, allowing for efficient uptake and a swift increase in the removal percentage [35,37].

However, as the initial concentration increases further (from 60 to 100 mg L^{-1}), the finite number of active binding domains, due to the fixed mass of adsorbent (0.2 mg mL^{-1}), become progressively saturated [37]. Once these specific sites are occupied, increasing the driving force yields diminishing returns as competition among the unabsorbed dye molecules intensifies [38]. This saturation limit decelerates the adsorption capacity and causes the observed decline in removal percentage as a larger fraction of MO molecules remains in the aqueous solution [37]. This concentration-dependent behavior is highly consistent with similar trends reported in the literature [35–37,39–41].

3.2.2. Effect of Cu_2O/CuO Nanoparticle Dosage

Figure 9 shows the effect of adsorbent dosage on the removal efficiency and adsorption capacity (q_e) of the nanocomposite. The experiments were conducted by varying the dosage from 0.1 to 1.6 mg mL^{-1} while keeping the initial dye concentration constant at 40 mg L^{-1} and pH at 6 for 180 min. As shown, the removal percentage increased significantly from 69.95% to 97.01% as the dosage varied from 0.1 to 1.0 mg mL^{-1}. This initial enhancement is directly linked to the proportional expansion of the total effective surface area and the introduction of a higher number of unsaturated active binding sites. Consequently, this greater availability facilitates a higher probability of successful interactions between the anionic dye molecules and the adsorbent surface [34,42,43]. Moreover, beyond the optimal dosage of 1.0 mg mL^{-1}, the removal efficiency reached a distinct plateau, demonstrating no further significant improvements despite the addition of more nanocomposite. This behavior suggests that the system reached a saturation threshold where almost all available MO molecules in the solution had already been captured. Conversely, the adsorption capacity (q_e) followed a continuous inverse trend, decreasing from 254.545 mg g^{-1} to 23.164 mg g^{-1} as the dosage increased. This phenomenon is primarily driven by the unsaturation of active sites at higher solid-to-liquid ratios. At low dosages, the high ratio of dye molecules to available sites leads to near-complete saturation of the adsorbent [44]. However, at higher dosages, the fixed amount of adsorbate becomes insufficient to occupy the surplus of active sites, leaving much of the material's surface unsaturated. Additionally, the decrease in q_e at higher concentrations can be linked to particle aggregation and overlapping of active sites, which reduce the effective surface area per unit mass and increase the intraparticle diffusion path length [45–47]. Therefore, 1.0 mg mL^{-1} was identified as the optimum dosage, representing the critical point where the maximum removal efficiency is achieved without excessively compromising the adsorption capacity per unit mass.

3.2.3. Effect of MO Solution pH and Point of Zero Charge of the Adsorbent

The point of zero charge (PZC) of the nanocomposite was determined using the pH drift method in order to analyze the adsorption mechanism as a function of pH [24]. As shown in Figure 10, the PZC was found to be 8.4, corresponding to the condition at which $\Delta pH = 0$. This result indicates that the surface of the material exhibits a net positive charge at pH values lower than 8.4 while it acquires a net negative charge at pH values above this

value, which directly influences the electrostatic interactions between the adsorbent and the adsorbate [48].

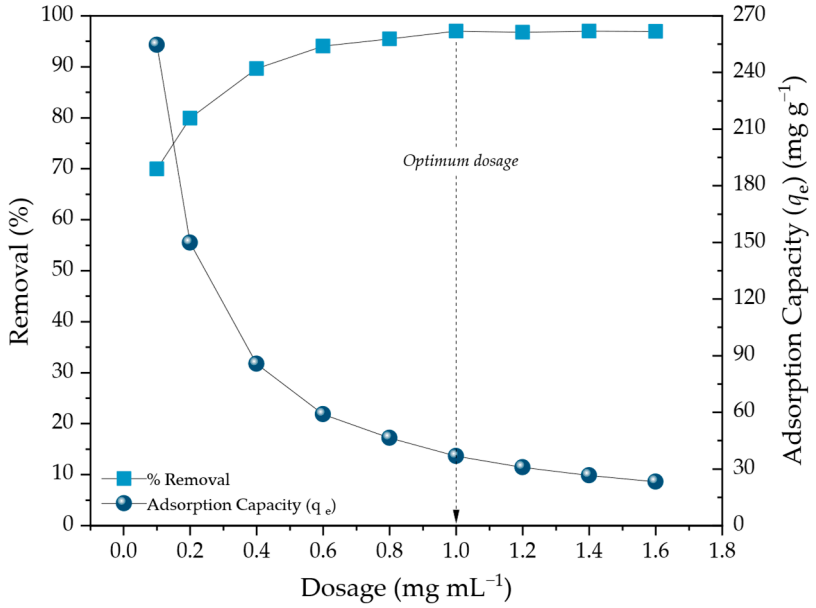

Figure 9. Removal percentage and adsorption capacity of Cu_2O/CuO nanoparticles at different nanocomposite doses.

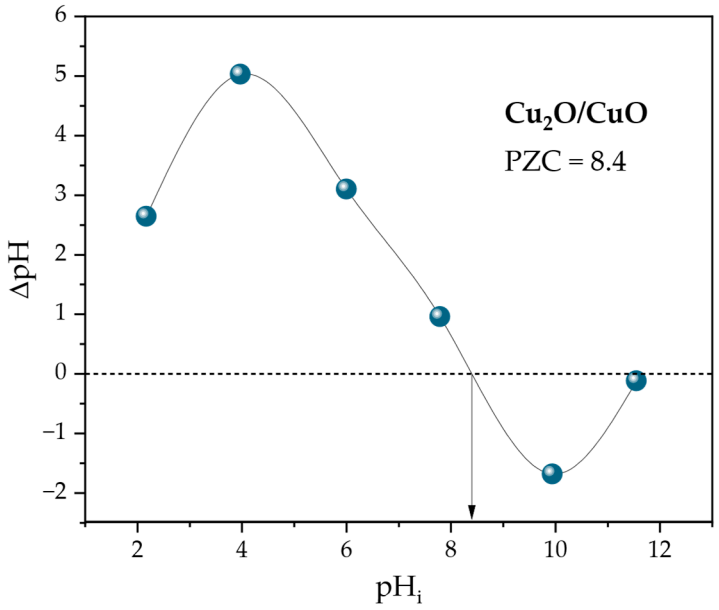

Figure 10. Point of zero charge (PZC) determination of the Cu_2O/CuO nanocomposite. The horizontal dashed line indicates ΔpH = 0.

The MO removal efficiency was evaluated by adjusting the pH of the solutions to 6, 9, 10, and 11 using 0.01 mol L^{-1} NaOH. The pH value of 6 corresponds to that of the original MO solution, and the initial dye concentration was kept constant at 40 mg L^{-1} and the adsorbent dosage was kept at 1.0 mg mL^{-1} over a period of 180 min. The results are presented in Figure 11. It was observed that the highest removal percentage was achieved at pH 6. This value can be directly explained by the results obtained as a function of the PZC position. Since the working pH of 6 is lower than the PZC = 8.4, the surface of the Cu_2O/CuO nanocomposite is positively charged as M-OH_2^+ [41]. This generates a strong electrostatic attraction with methyl orange molecules, which, being an anionic dye

with sulfonate groups (SO_3^-), are effectively attracted to the adsorbent surface [30,49]. In contrast, when the pH increased to alkaline values of 9, 10, and 11, the removal efficiency dropped drastically to values close to zero. This occurs because when the PZC value of 8.4 is exceeded, the surface of the adsorbent becomes deprotonated and acquires a negative charge (M-O^-) [41,48]. Since both the adsorbent and the dye possess the same negative charge, strong electrostatic repulsion occurs, hindering adsorption [30,33]. In addition, during the evaluation at different pH values, it is inferred that there is significant competition between excess hydroxyl ions (OH^-) and dye ions for the active sites [48,49].

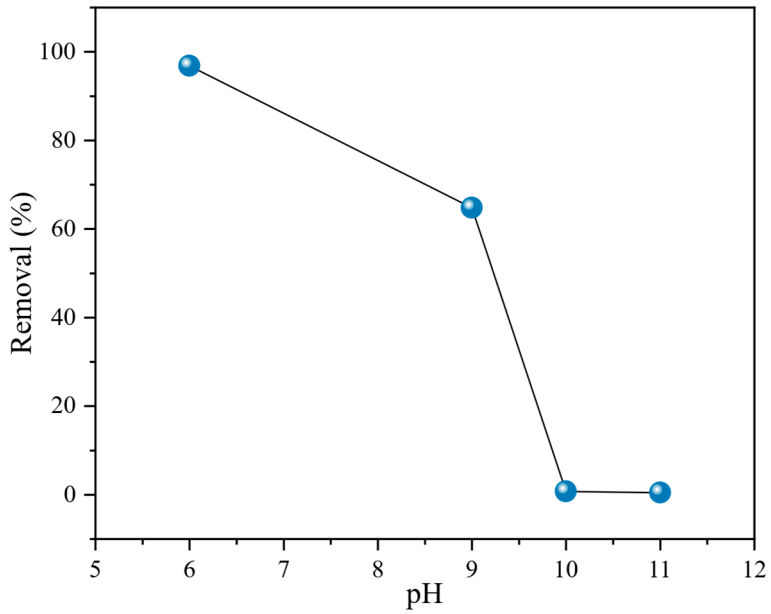

Figure 11. Removal percentage of Cu_2O/CuO nanoparticles at different pH values. The dots represent experimental data, and the solid line connects the points to guide the eye.

3.2.4. Effect of Contact Time

Figure 12 shows the adsorption kinetics of MO under the previously optimized conditions over a period of up to 300 min. In the initial stage, within the first 40 min, rapid dye uptake was recorded, reaching an adsorption capacity (q_e) of 29.930 mg g^{-1}. This initial behavior is attributed to the high availability of vacant active sites and the large concentration gradient between the solution and the adsorbent, which drives efficient mass transfer toward the solid surface [17,22]. As contact time increases, the adsorption rate gradually decreases. This deceleration is due to the progressive saturation of surface active sites, which generates steric resistance, and to the increase in electrostatic repulsion between the MO molecules already adsorbed and those remaining in solution [20,22]. Finally, the system reaches dynamic equilibrium at 180 min, achieving a maximum adsorption capacity (q_e) of 36.713 mg g^{-1}. Notably, this equilibrium time is significantly shorter than the 540 and 720 min reported for CuO and NiO nanoparticles, respectively [18], and the 260 min required by mesoporous zeolites [22], highlighting the potential of the developed methodology for dye removal in aqueous media.

3.2.5. Total Organic Carbon (TOC) Analysis

To confirm total removal of MO by the Cu_2O/CuO nanocomposite, the Total Organic Carbon assay (TOC) was conducted. After 180 min of treatment using an MO solution (40 mg L^{-1}) and a nanocomposite dosage of 1.0 mg mL^{-1}, the assay revealed a decrease from an initial concentration of 23.6 mg L^{-1} to 10.8 mg L^{-1}, corresponding to a 54.2% reduction in Total Organic Carbon. The significant discrepancy between the UV–Vis

decolorization efficiency (97.0%) and the actual TOC reduction (51.1%) indicates a dual removal mechanism. While the rapid cleavage of the azo bonds results in substantial optical decolorization, a significant fraction of the dye is converted into colorless intermediate byproducts that remain dissolved in the aqueous phase. We anticipate that extending the contact time could increase the mineralization of these intermediate products [50,51].

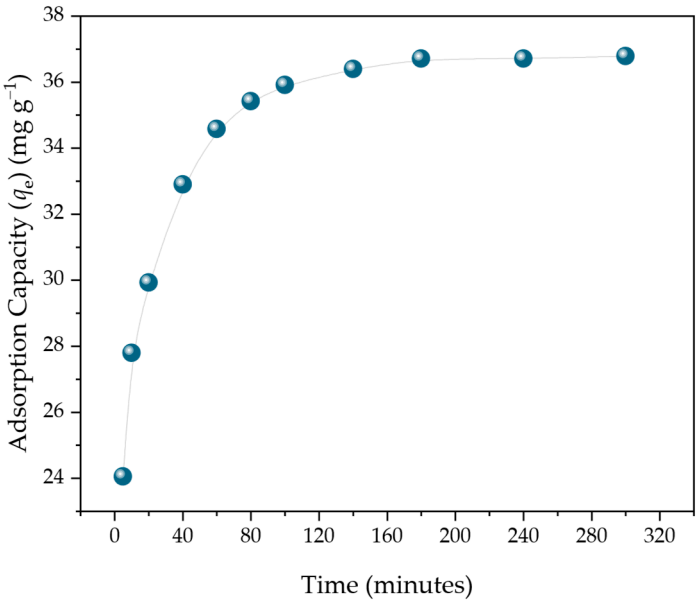

Figure 12. Effect of contact time on the adsorption capacity (q_e) of the Cu_2O/CuO nanocomposite. The dots represent experimental data, and the solid line connects the points to guide the eye.

3.3. Adsorption Kinetics

The adsorption kinetics of the Cu_2O/CuO nanocomposite were studied to investigate the adsorption mechanism and rate. The models used were the pseudo-first-order (PFO), pseudo-second-order (PSO), and intraparticle diffusion models [33,38,52]. The non-linear forms of these models are shown below.

Pseudo-first-order model:

$$q_t = q_e(1 - e^{-k_1 t}) \quad (4)$$

Pseudo-second-order model:

$$q_t = \frac{q_e^2 K_2 t}{1 + q_e K_2 t} \quad (5)$$

Intraparticle diffusion model:

$$q_t = K_{ip} t^{0.5} + t \quad (6)$$

where qe and q_t (mg g^{-1}) indicate the amounts of dye adsorbed at equilibrium and at time t (min), respectively; K_1 (min^{-1}) and K_2 (g mg^{-1} min^{-1}) represent the pseudo-first-order and pseudo-second-order rate constants, respectively; and K_{ip} (mg g^{-1} min$^{0.5}$) is the intraparticle diffusion coefficient.

To quantify the changes and determine the reaction order, the experimental data were fitted to the pseudo-first-order and pseudo-second-order models, whose non-linear fittings are shown in Figure 13a. The kinetic parameters calculated from the slopes and intercepts of these plots, as well as the determination coefficients (R^2), and three statistical error functions (chi-square (χ^2), root mean square error (RMSE), and standard error (SE)) are summarized in Table 1.

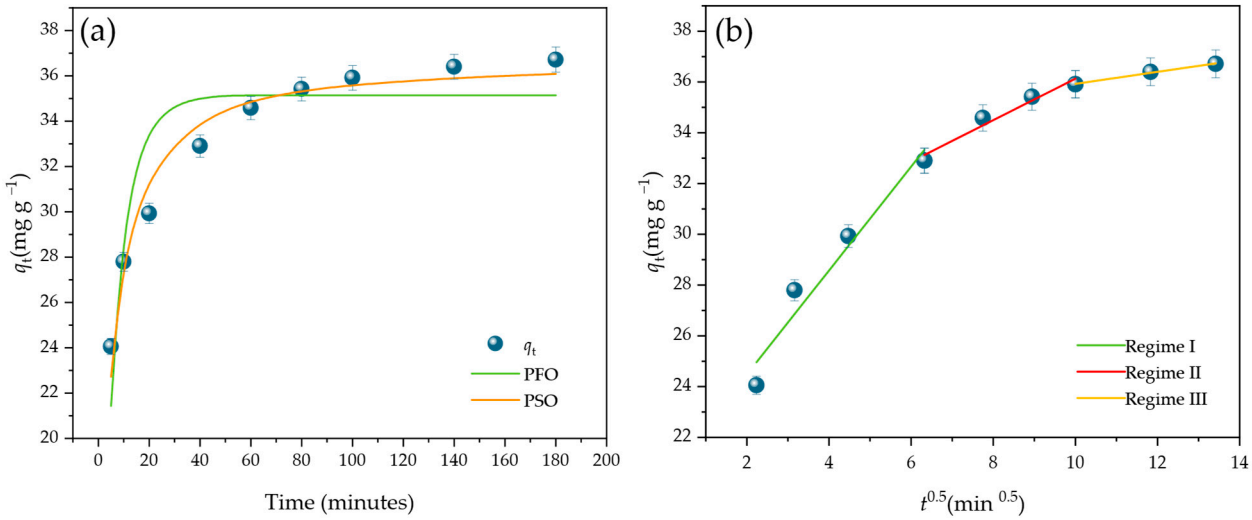

Figure 13. (**a**) Pseudo-first-order and pseudo-second-order kinetic model for MO adsorption onto the Cu_2O/CuO nanocomposite under dark conditions. (**b**) Weber–Morris intraparticle diffusion model.

Table 1. Pseudo-first-order and pseudo-second-order kinetic parameters of the Cu_2O/CuO nanocomposite.

Model	Parameter	Value
Pseudo-first order (PFO)	$q_{e(cal)}$ (mg g^{-1})	34.62
	K_1 (g mg^{-1} min^{-1})	0.197
	R^2	0.7557
	χ^2	1.233
	RMSE	2.067
	SE	2.193
Pseudo-second order (PSO)	$q_{e(cal)}$ (mg g^{-1})	36.48
	K_2 (g mg^{-1} min^{-1})	0.009
	R^2	0.9530
	χ^2	0.245
	RMSE	0.908
	SE	0.963

By analyzing the values in Table 1, it is observed that the pseudo-first-order model presented a weak correlation value (R^2 = 0.7557) alongside relatively high error analysis parameters (χ^2 = 1.233, RMSE = 2.067, and SE = 2.193). Although its theoretically calculated adsorption capacity ($q_{e(cal)}$ = 34.62 mg g^{-1}) is close to the experimental value ($q_{e(exp)}$ = 36.71), the poor linear fitting for the PFO indicates that the adsorption of MO onto the nanocomposite does not strictly follow first-order kinetics. In contrast, the pseudo–second-order model showed a better linear fit, with a strong correlation coefficient (R^2 = 0.9530) and significantly lower error values (χ^2 = 0.245, RMSE 0.908, and SE = 0.963). In addition, the value of $q_{e(cal)}$ = 36.48 mg g^{-1} agrees well with the experimental value. These results confirm that the adsorption kinetics are better described by the PSO model, which suggests that chemisorption is the rate-limiting step [53]. This implies that the adsorption forces involve electron exchange between the anionic sulfonate groups of the MO and the cationic active sites of the copper oxide [43].

Finally, to identify whether diffusion within the pores is the rate-limiting factor, the Weber–Morris intraparticle diffusion model [54], shown in Figure 13b and Table 2, was applied. According to this model, if the linear regression passes through the origin, intraparticle diffusion is the sole rate-limiting step [24]. The intraparticle diffusion model exhibited a multi-linear profile with three adsorption regions. The first stage, regime I

(0–40 min), presented the steepest slope (K_{ip} = 2.047 mg g^{-1} $min^{-0.5}$) and a positive intercept (C = 20.384 mg g^{-1}), suggesting that boundary layer diffusion or external surface adsorption makes a very important contribution to the initial rate of the process, acting simultaneously with intraparticle diffusion [24,29]. While the linear fit (R^2 = 0.9509) for this stage is strong, it may hint at a chaotic and complex mass transfer process. Once the external sites become saturated, the process moved to regime II (40–100 min), which was accompanied by a decrease in the slope (K_{ip} = 0.818 mg g^{-1} $min^{-0.5}$). This stage corresponds to the intraparticle diffusion, where the MO molecules navigate the internal porous structure of the nanocomposite and the higher interceptive value (C = 27.954 mg g^{-1}) suggests that boundary layer thickness may exert a strong effect on the mass transfer. The correlation improved for this stage (R^2 = 0.9602). Finally, regime III (100–180 min) showed an even flatter slope (K_{ip} = 0.236 mg g^{-1} $min^{-0.5}$). This final phase is characterized by a notable reduction in the adsorption rate accompanied by a strong correlation value (R^2 = 0.9931).

Table 2. Kinetic parameters of Weber–Morris intraparticle diffusion model for the Cu_2O/CuO nanocomposite.

Kinetic Regime	Time Range (min)	K_{ip} (mg g^{-1} $min^{-0.5}$)	C (mg g^{-1})	R^2
Regime I	0–40	2.047	20.384	0.9509
Regime II	40–100	0.818	27.954	0.9602
Regime III	100–180	0.236	33.565	0.9931

3.4. Adsorption Isotherms

Adsorption isotherms are essential for evaluating the efficiency of the adsorption process, describing how adsorbate molecules interact with the adsorbent surface, and can be used to determine the theoretical maximum capacity of the material. Furthermore, fitting experimental data to isothermal models provides valuable information regarding the adsorption behavior and its underlying mechanisms [55]. In this study, experimental equilibrium data were evaluated using the Langmuir, Freundlich, and Langmuir–Freundlich models. The Langmuir model assumes that adsorption occurs at specific homogeneous sites within the adsorbent without lateral interaction between the adsorbed molecules, whereas the Freundlich model characterizes adsorption on a heterogeneous surface [56]. The Langmuir–Freundlich model combines both approaches to describe complex heterogeneous systems. To accurately model the adsorption process, the experimental data were fitted using non-linear optimization. This method offers a more reliable mathematical approach for estimating the adsorption parameters as it minimizes the error distribution and strictly preserves the original form of the isothermal equations [57]. These non-linear models can be mathematically represented as follows [37,38,52,57]:

Langmuir model:

$$q_e = q_{max}\frac{K_L C_e}{1 + K_L C_e} \quad (7)$$

Freundlich model:

$$q_e = K_F C_e^{1/n} \quad (8)$$

Langmuir–Freundlich model:

$$q_e = \frac{q_{max}(K_{LF}C_e)^{M_{LF}}}{1 + (K_{LF}C_e)^{M_{LF}}} \quad (9)$$

where C_e (mg L^{-1}) denotes the residual dye concentration at equilibrium; q_e and q_m (mg g^{-1}) correspond to the adsorption capacity at equilibrium and the maximum monolayer capacity, respectively; K_L (L mg^{-1}) represents the Langmuir constant related to the

affinity between the adsorbate and the adsorbent; and K_F (L mg^{-1}) and n are the Freundlich model constants, with n indicating the intensity and favorability of the process. For the Langmuir–Freundlich model, K_{LF} (L mg^{-1}) is the affinity constant and M_{LF} represents the heterogeneity index of the adsorbent surface.

To investigate the surface characteristics of the Cu_2O/CuO nanocomposite and the distribution behavior of MO on its surface, adsorption isotherm models were employed. The experimental equilibrium data were analyzed using non-linear regression methods for two-parameter (Langmuir and Freundlich) and three-parameter (Langmuir–Freundlich) models. The accuracy of each model was comprehensively assessed and compared using the coefficient of determination (R^2) and three statistical error functions: chi-square (χ^2), root mean square error (RMSE), and standard error (SE). The non-linear representations are illustrated in Figure 14, and the associated model parameters are summarized in Table 3.

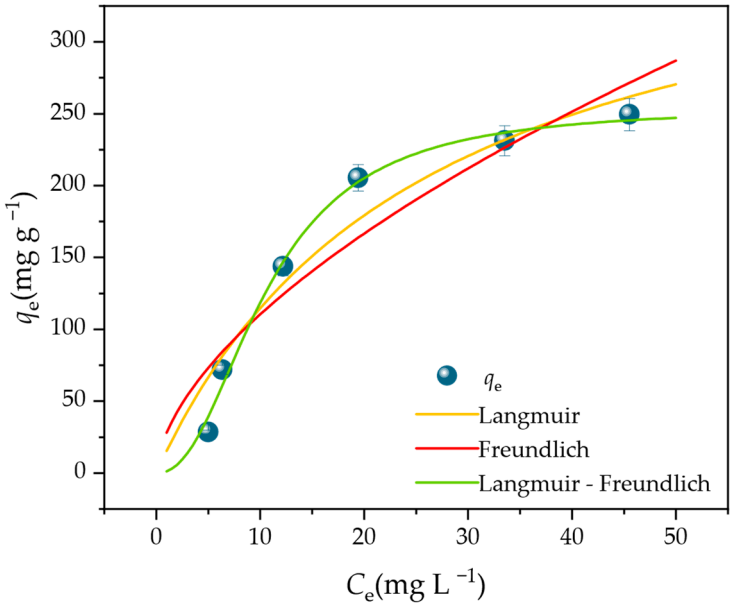

Figure 14. Adsorption isotherm models: Langmuir, Freundlich and Langmuir–Freundlich for MO adsorption onto the Cu_2O/CuO nanocomposite (adsorbent dose = 0.2 mg mL^{-1}, and pH = 6).

The data presented in Table 3 provide key insights into the performance of the non-linear forms of the evaluated models. Among the two-parameter models, Langmuir exhibited better performance than Freundlich, demonstrating a stronger correlation (R^2 = 0.9331) and lower error values (χ^2 = 29.532; RMSE = 23.232; SE = 25.232). However, this model failed to accurately describe the MO adsorption onto the Cu_2O/CuO NPs as it substantially overestimated the calculated maximum monolayer adsorption capacity (q_{max} = 409.661 mg g^{-1}) compared to the experimental value. Conversely, the Freundlich model failed to adequately describe the system owing to the significant deviation between the experimental and calculated data, as reflected by its low correlation (R^2 = 0.8813) and the highest error metrics (χ^2 = 44.752; RMSE = 30.940; SE = 34.592).

In contrast, the calculation of error functions and the coefficient of determination clearly indicates that the three-parameter Langmuir–Freundlich model provides the most suitable framework for modeling the equilibrium sorption data. This model exhibited a strong correlation value (R^2 = 0.9922), demonstrating that it accounts for nearly all variability in the measured equilibrium concentrations. Furthermore, the precision of the Langmuir–Freundlich model's estimates was validated by the exceptionally low values of the error metrics (χ^2 = 5.504; RMSE = 7.950; SE = 10.264). Considering the large range of the observed q_e values (ranging from 28.50 to 249.48 mg g^{-1}), this minor discrepancy

highlights the robustness of the fit. The identical SE value underscores the tight clustering of experimental data points (q_e) around the predicted values of the model.

Table 3. Parameters of the Langmuir, Freundlich and Langmuir–Freundlich adsorption isotherm models for MO removal using Cu_2O/CuO.

Isotherm Model	Parameter	Value
Langmuir	q_{max} (mg g^{-1})	409.661
	K_L (L mg^{-1})	0.039
	R^2	0.9331
	χ^2	29.532
	RMSE	23.232
	SE	25.232
Freundlich	K_F (L mg^{-1})	28.145
	1/n	0.594
	R^2	0.8813
	χ^2	44.752
	RMSE	30.94
	SE	34.592
Langmuir–Freundlich	q_{max} (mg g^{-1})	254.759
	K_{LF} (L mg^{-1})	0.094
	M_{LF}	2.252
	R^2	0.9922
	χ^2	5.504
	RMSE	7.95
	SE	10.264

Crucially, the Langmuir–Freundlich model accurately predicted a maximum adsorption capacity (q_{max}) of 254.759 mg g^{-1}, which aligns closely with the maximum experimental value obtained (249.48 mg g^{-1}). This superior fit, characterized by an affinity constant (K_{LF}) of 0.094 L mg^{-1} and a heterogeneity index (M_{LF}) of 2.252, reinforces the surface heterogeneity hypothesis [37,38]. Because the M_{LF} value significantly deviates from unity, it confirms the presence of diverse adsorption sites with varying affinities on the nanocomposite surface. Therefore, the adsorption process occurs on an energetically heterogeneous surface, combining elements of monolayer saturation at high concentrations and multilayer formation driven by highly active sites at lower concentrations [37]. The adsorption capacity obtained in this study is substantially higher than the values reported for other Cu_2O/CuO-based adsorbents in the literature (as tabulated in Table 4), indicating a strong affinity and significantly enhanced MO uptake.

Table 4. Kinetic and adsorption parameters of different adsorbents for MO.

Adsorbent	Best Model	K_2 (g mg min)	Dosage (mg mL^{-1})	pH	MO (mg L^{-1})	q_e (mg g^{-1})	Ref.
Biochar from chicken manure	Pseudo-second order	0.0107	1	6.5	25–75	41.49	[16]
Organic matter-rich clays from Egypt (OMRC)	Pseudo-second order	0.094	4	2	60–140	41.67	[17]
Calcinated organic matter-rich clays from Egypt (COMRC)	Pseudo-second order	0.037	4	2	60–140	34.48	[17]
Activated carbon	Pseudo-second order	0.0003793	-	2	100	100	[33]

Table 4. *Cont.*

Adsorbent	Best Model	K_2 (g mg min)	Dosage (mg mL^{-1})	pH	MO (mg L^{-1})	q_e (mg g^{-1})	Ref.
CuO NPs	Pseudo-second order	0.02441	2	-	200–1000	217.40	[18]
NiO NPs	Pseudo-second order	0.00024	2	-	200–1000	370.40	[18]
Co_3O_4 NPs	Pseudo-second order	20.823	10	6	50	46.08	[20]
Mesoporous ZSM-5 zeolite	Pseudo-second order	0.01860	2.4	-	10	5.50	[22]
Cu_2O particles	-	-	2	-	10–80	96.42	[21]
Cu_2O/CuO	Pseudo-second order	0.009	0.2	6	10–100	249.48	This work

3.5. Comparison with Other Materials

As shown in Table 4 of kinetic and adsorption parameters, the Cu_2O/CuO nanocomposite exhibits an adsorption capacity comparable to, and even higher than, that of previously reported modified materials. It is important to highlight the efficiency per unit mass of this system as it achieves these results using optimized parameters, including a minimal and comparable adsorbent dose. Although studies such as Darwish et al. [18] report higher maximum adsorption capacities (q_{max}), these are conditioned by high initial concentrations of methyl orange, which force saturation, unlike the conditions evaluated in this work. The nanocomposite was also evaluated against other materials, with results indicating that the pseudo-second-order model provided the most accurate representation. On the other hand, Table 5 highlights the kinetic efficiency of Cu_2O/CuO. The material achieved 97.0% removal in only 180 min, outperforming others in both time and efficiency. This work achieved better results than adsorbents using doses eight times higher (4 mg mL^{-1}), which only reached 50% removal [32]. Although this method requires light conditions, it suggests excellent dual potential and could exhibit superior performance in coupled photocatalytic processes.

Table 5. Percentage of MO removal of different photocatalysts under visible light.

Material	Dosage (mg mL^{-1})	pH	MO (mg L^{-1})	Time (h)	Removal (%)	Ref.
TiO_2/Carbon	0.6	-	10	24	90.0	[58]
CuO NPs	0.9	6.5	45	6	84.9	[41]
80%CuO/Cu_2O	4	-	5	3	50.0	[32]
90%CuO/Cu_2O	4	-	5	3	19.0	[32]
RGO/Cu_2O	1	-	10	3.7	96.1	[59]
Cu_2O NPs	0.2		20	4.5	40.0	[27]
Cu_2O/CuO	1	6	40	3	97.0	This work

4. Conclusions

In the present study, Cu_2O/CuO nanoparticles were successfully synthesized via liquid-phase chemical precipitation, obtaining quasi-spherical nanoparticles with an average size of ~18 nm, SSA of 19.54 m^2 g^{-1} and total pore volume of 0.103 cm^3 g^{-1}. UV-Vis spectroscopy revealed a 97.0% degradation efficiency for methyl orange in aqueous solution after 180 min. The TOC content assay of the treated dye sample revealed a 54.2% reduction in carbon content, which indicates conversion of the dye into colorless intermediates and mineralization.

Operating at pH 6 (below the PZC of 8.4) facilitated the electrostatic capture of the dye by protonated surface hydroxyls, while cationic copper centers drive a pseudo-second-order chemisorption process. The system is best described by the Langmuir–Freundlich model, reflecting a highly heterogeneous distribution of active sites. This indicates a cooperative adsorption mechanism where multilayer coverage at lower dye concentrations transitions into a saturated monolayer at higher concentrations, ultimately culminating in a high maximum experimental adsorption capacity of 249.48 mg g^{-1}.

These findings support the potential of the Cu_2O/CuO nanoparticle system as a promising alternative for the environmental remediation of textile effluents.

Author Contributions: Conceptualization, Y.A.-A., A.S. and R.R.-C.; methodology, Y.A.-A. and A.S.; Software, Y.A.-A., A.S. and A.H.; validation, M.R. and A.H.; formal analysis, Y.A.-A. and A.S.; investigation, Y.A.-A., A.S. and R.R.-C.; resources, R.G. and R.R.-C.; writing—original draft preparation, Y.A.-A.; writing—review and editing, Y.A.-A., A.S. and R.R.-C.; visualization, Y.A.-A. and A.S.; supervision, R.G. and M.R.; project administration, R.G. and R.R.-C.; funding acquisition, R.G. and R.R.-C. All authors have read and agreed to the published version of the manuscript.

Funding: This research was funded by the Universidad Nacional de San Agustin de Arequipa, grant number PI-005-2023-UNSA. The APC was funded by PI-005-2023-UNSA.

Institutional Review Board Statement: Not applicable.

Informed Consent Statement: Not applicable.

Data Availability Statement: The data presented in this study are available on request from the corresponding author. The data are not publicly available due to privacy.

Acknowledgments: The authors sincerely thank the Laboratorio de Caracterización Funcional de Materiales (LCFM) and Centro de Investigación Aplicada y Laboratorios Especializados (CIALE), for providing the facilities and technical support.

Conflicts of Interest: The authors declare no conflicts of interest.

Abbreviations

The following abbreviations are used in this manuscript:

MO	Methyl orange
PZC	Point of zero charge
PVP	Polyvinylpyrrolidone
AA	L-ascorbic acid
PFO	Pseudo-first order
PSO	Pseudo-second order
SSA	Specific surface area

References

1. Al-Tohamy, R.; Ali, S.S.; Li, F.; Okasha, K.M.; Mahmoud, Y.A.-G.; Elsamahy, T.; Jiao, H.; Fu, Y.; Sun, J. A Critical Review on the Treatment of Dye-Containing Wastewater: Ecotoxicological and Health Concerns of Textile Dyes and Possible Remediation Approaches for Environmental Safety. *Ecotoxicol. Environ. Saf.* **2022**, *231*, 113160. [CrossRef]
2. Iwuozor, K.O.; Ighalo, J.O.; Emenike, E.C.; Ogunfowora, L.A.; Igwegbe, C.A. Adsorption of Methyl Orange: A Review on Adsorbent Performance. *Curr. Res. Green Sustain. Chem.* **2021**, *4*, 100179. [CrossRef]
3. Kangralkar, M.V.; Kangralkar, V.A.; Manjanna, J. Adsorption of Cr (VI) and Photodegradation of Rhodamine b, Rose Bengal and Methyl Red on Cu_2O Nanoparticles. *Environ. Nanotechnol. Monit. Manag.* **2021**, *15*, 100417. [CrossRef]
4. Guo, R.; Chang, J.; Li, H.; He, J.; Pan, P.; Yang, Z.; Wei, J. Preparation of 26-Facet Cu_2O@Cu Composite and Its Methyl Orange Adsorption Behavior. *J. Alloys Compd.* **2022**, *895*, 162630. [CrossRef]
5. Ranaweera, R.W.; Jayaweera, V.; De Silva, N.; Wijesekara, H.; Gunatilake, S.; Mubarak, A.; Sandaruwan, C. Synthesis of Nano Zero Valent Zinc-Reduced Graphene Oxide Nanocomposite Using a Novel Electrochemical Technique for the Adsorptive Degradation of Methyl Orange. *Colloids Surf. A Physicochem. Eng. Asp.* **2024**, *703*, 135250. [CrossRef]

6. Adeel, M.; Saeed, M.; Khan, I.; Muneer, M.; Akram, N. Synthesis and Characterization of Co–ZnO and Evaluation of Its Photocatalytic Activity for Photodegradation of Methyl Orange. *ACS Omega* **2021**, *6*, 1426–1435. [CrossRef] [PubMed]
7. Fradj, A.B.; Boubakri, A.; Hafiane, A.; Hamouda, S. Ben Removal of Azoic Dyes from Aqueous Solutions by Chitosan Enhanced Ultrafiltration. *Results Chem.* **2020**, *2*, 100017. [CrossRef]
8. Lau, Y.-Y.; Wong, Y.-S.; Teng, T.-T.; Morad, N.; Rafatullah, M.; Ong, S.-A. Degradation of Cationic and Anionic Dyes in Coagulation–Flocculation Process Using Bi-Functionalized Silica Hybrid with Aluminum-Ferric as Auxiliary Agent. *RSC Adv.* **2015**, *5*, 34206–34215. [CrossRef]
9. Wadhawan, G.; Gupta, A. Biological Treatment of Methyl Orange Dye and Textile Wastewater Using Halo-Alkaliphilic Bacteria under Highly Alkaline Conditions. *Extremophiles* **2025**, *29*, 6. [CrossRef]
10. Crini, G. Non-Conventional Low-Cost Adsorbents for Dye Removal: A Review. *Bioresour. Technol.* **2006**, *97*, 1061–1085. [CrossRef]
11. Sahu, A.; Poler, J.C. Removal and Degradation of Dyes from Textile Industry Wastewater: Benchmarking Recent Advancements, Toxicity Assessment and Cost Analysis of Treatment Processes. *J. Environ. Chem. Eng.* **2024**, *12*, 113754. [CrossRef]
12. Satyam, S.; Patra, S. Innovations and Challenges in Adsorption-Based Wastewater Remediation: A Comprehensive Review. *Heliyon* **2024**, *10*, e29573. [CrossRef]
13. Farastoon Dashti, S.S.; Ansari, I.; Emamshoushtari, M.M.; Helchi, S.; Lessage, G.; Heran, M.; Pajoum Shariati, F. Comparison of Batch and Continuous Operation Modes for Maxilon Red Azo Dye Removal Using Chlorella Vulgaris Microalgae within Photobioreactor (PBR) and a Dynamic Membrane Photobioreactor (DMPBR). *Front. Membr. Sci. Technol.* **2025**, *4*, 1653159. [CrossRef]
14. Solayman, H.M.; Hossen, M.A.; Abd Aziz, A.; Yahya, N.Y.; Leong, K.H.; Sim, L.C.; Monir, M.U.; Zoh, K.-D. Performance Evaluation of Dye Wastewater Treatment Technologies: A Review. *J. Environ. Chem. Eng.* **2023**, *11*, 109610. [CrossRef]
15. Zakir, O.; Ait-Karra, A.; Khardazi, S.; Idouhli, R.; Khadiri, M.E.; Dikici, B.; Aboulaich, A.; Outzourhit, A.; Abouelfida, A. Recent Progress in Nanomaterials for Water Treatment: A Comprehensive Review of Adsorption, Photocatalytic, and Antibacterial Applications. *J. Water Process Eng.* **2025**, *72*, 107566. [CrossRef]
16. Yu, J.; Zhang, X.; Wang, D.; Li, P. Adsorption of Methyl Orange Dye onto Biochar Adsorbent Prepared from Chicken Manure. *Water Sci. Technol.* **2018**, *77*, 1303–1312. [CrossRef]
17. Zayed, A.M.; Abdel Wahed, M.S.M.; Mohamed, E.A.; Sillanpää, M. Insights on the Role of Organic Matters of Some Egyptian Clays in Methyl Orange Adsorption: Isotherm and Kinetic Studies. *Appl. Clay Sci.* **2018**, *166*, 49–60. [CrossRef]
18. Darwish, A.A.A.; Rashad, M.; AL-Aoh, H.A. Methyl Orange Adsorption Comparison on Nanoparticles: Isotherm, Kinetics, and Thermodynamic Studies. *Dye. Pigment.* **2019**, *160*, 563–571. [CrossRef]
19. Sasmal, A.K.; Pal, J.; Sahoo, R.; Kartikeya, P.; Dutta, S.; Pal, T. Superb Dye Adsorption and Dye-Sensitized Change in Cu_2O–Ag Crystal Faces in the Dark. *J. Phys. Chem. C* **2016**, *120*, 21580–21588. [CrossRef]
20. Uddin, M.K.; Baig, U. Synthesis of Co_3O_4 Nanoparticles and Their Performance towards Methyl Orange Dye Removal: Characterisation, Adsorption and Response Surface Methodology. *J. Clean. Prod.* **2019**, *211*, 1141–1153. [CrossRef]
21. Ho, W.; Tay, Q.; Qi, H.; Huang, Z.; Li, J.; Chen, Z. Photocatalytic and Adsorption Performances of Faceted Cuprous Oxide (Cu_2O) Particles for the Removal of Methyl Orange (MO) from Aqueous Media. *Molecules* **2017**, *22*, 677. [CrossRef]
22. Radoor, S.; Karayil, J.; Jayakumar, A.; Parameswaranpillai, J.; Siengchin, S. Efficient Removal of Methyl Orange from Aqueous Solution Using Mesoporous ZSM-5 Zeolite: Synthesis, Kinetics and Isotherm Studies. *Colloids Surf. A Physicochem. Eng. Asp.* **2021**, *611*, 125852. [CrossRef]
23. Zhao, J.; Yuan, S.; Wang, H.; Guo, Q.; Tian, H. Bifunctional Catalysts AC/Cu_2O/CuO for Removal of Organic Pollutant with Enhanced Visible Light Photocatalysis. *Chem. Phys. Impact* **2021**, *3*, 100041. [CrossRef]
24. Dutta, S.K.; Amin, M.K.; Ahmed, J.; Elias, M.; Mahiuddin, M. Removal of Toxic Methyl Orange by a Cost-Free and Eco-Friendly Adsorbent: Mechanism, Phytotoxicity, Thermodynamics, and Kinetics. *S. Afr. J. Chem. Eng.* **2022**, *40*, 195–208. [CrossRef]
25. Hua, M.; Zhang, S.; Pan, B.; Zhang, W.; Lv, L.; Zhang, Q. Heavy Metal Removal from Water/Wastewater by Nanosized Metal Oxides: A Review. *J. Hazard. Mater.* **2012**, *211–212*, 317–331. [CrossRef]
26. Liao, H.; Wang, Z. Adsorption Removal of Amaranth by Nanoparticles-Composed Cu_2O Microspheres. *J. Alloys Compd.* **2018**, *769*, 1088–1095. [CrossRef]
27. Plascencia-Hernández, F.; Luna, A.L.; Colbeau-Justin, C.; Santiago, P.; Garcia-Rocha, M.; Valverde-Aguilar, G.; Valenzuela, M.A. Cu_2O Cubic and Polyhedral Structures versus Commercial Powder: Shape Effect on Photocatalytic Activity under Visible Light. *J. Saudi Chem. Soc.* **2019**, *23*, 1016–1023. [CrossRef]
28. Huang, L.; Peng, F.; Yu, H.; Wang, H. Synthesis of Cu_2O Nanoboxes, Nanocubes and Nanospheres by Polyol Process and Their Adsorption Characteristic. *Mater. Res. Bull.* **2008**, *43*, 3047–3053. [CrossRef]
29. Peng, Y.; Feng, Y.; Tao, Y.; Wan, H. Preparation of Nanoparticles-Assembled Cu_2O Microspheres by Ultrasound- Assisted Polyol Process and Their Adsorption Performance. *Desalination Water Treat.* **2022**, *270*, 236–244. [CrossRef]
30. Mrunal, V.K.; Vishnu, A.K.; Momin, N.; Manjanna, J. Cu_2O Nanoparticles for Adsorption and Photocatalytic Degradation of Methylene Blue Dye from Aqueous Medium. *Environ. Nanotechnol. Monit. Manag.* **2019**, *12*, 100265. [CrossRef]

31. Zhang, Y.; Wang, D.; Zhang, X.; Qu, F. Template-Free Synthesis of Porous Cu_2O Nanospheres at Room Temperature and Investigation on Their Adsorption Property. *J. Nanomater.* **2013**, *2013*, 378919. [CrossRef]
32. Bayat, F.; Sheibani, S. Enhancement of Photocatalytic Activity of CuO-Cu_2O Heterostructures through the Controlled Content of Cu_2O. *Mater. Res. Bull.* **2022**, *145*, 111561. [CrossRef]
33. Dehmani, Y.; Franco, D.S.P.; Georgin, J.; Mghaiouini, R.; Mohammed, B.B.; Kacimi, R.; Lamhasni, T.; Lima, E.C.; El Messaoudi, N.; Sadik, A. Towards a Deeper Understanding of the Adsorption of Methyl Orange on a Commercial Activated Carbon: Study of Impact Factors, Isotherm and Mechanism. *Environ. Surf. Interfaces* **2025**, *3*, 103–111. [CrossRef]
34. Abbasi, A.; Khatoon, F.; Ikram, S. A Review on Remediation of Dye Adulterated System by Ecologically Innocuous "Biopolymers/Natural Gums-Based Composites". *Int. J. Biol. Macromol.* **2023**, *231*, 123240. [CrossRef]
35. Essa, W.K. Methylene Blue Removal by Copper Oxide Nanoparticles Obtained from Green Synthesis of Melia Azedarach: Kinetic and Isotherm Studies. *Chemistry* **2024**, *6*, 249–263. [CrossRef]
36. Al-Bayati, R.A.; Ahmed, A.S.; Jaber, S.H.; Ali, D.A. Removal of Safranin-O Dye from an Aqueous Solution Using a Synthesized Copper Oxide Nanoparticles Doped by Silver: Thermodynamic and Kinetic Study. *Results Chem.* **2026**, *20*, 103060. [CrossRef]
37. Shehata, N.; Singh, S.; Varshney, R.; N, P.; Dhanjal, D.S.; Ramamurthy, P.C. Plant-Extract-Mediated Synthesis of Copper Oxide Nanoparticles for Sustainable Lead Detoxification: Experimental Evaluation and Docking Studies. *Nanoscale Adv.* **2026**, *8*, 1762–1775. [CrossRef]
38. EL-Hashani, A.; Amer, H.; Edbey, K.; Bhattarai, A. Xanthated Arbutus Pavarii Leaves as a Novel Biosorbent for Methyl Violet 6B: A Comparative Nonlinear Regression Approach for Kinetic Isotherm, and Thermodynamic Modeling. *Results Chem.* **2026**, *20*, 102976. [CrossRef]
39. Salleh, M.A.M.; Mahmoud, D.K.; Karim, W.A.W.A.; Idris, A. Cationic and Anionic Dye Adsorption by Agricultural Solid Wastes: A Comprehensive Review. *Desalination* **2011**, *280*, 1–13. [CrossRef]
40. Gebremedhin, K.H.; Gebreegziabher, H.G.; Weldegebrieal, G.K.; Ali, Y.M. Synergistic Adsorption-Photocatalysis Effect of CuO/TiO_2 Composite for High-Efficient Degradation of Methyl Orange. *Discov. Nano* **2025**, *20*, 209. [CrossRef] [PubMed]
41. Alhalili, Z. Green Synthesis of Copper Oxide Nanoparticles CuO NPs from Eucalyptus Globoulus Leaf Extract: Adsorption and Design of Experiments. *Arab. J. Chem.* **2022**, *15*, 103739. [CrossRef]
42. Liang, Y.-P.; Chan, Y.-B.; Aminuzzaman, M.; Shahinuzzaman, M.; Djearamane, S.; Thiagarajah, K.; Leong, S.-Y.; Wong, L.-S.; Tey, L.-H. Green Synthesis and Characterization of Copper Oxide Nanoparticles from Durian (*Durio zibethinus*) Husk for Environmental Applications. *Catalysts* **2025**, *15*, 275. [CrossRef]
43. Aroob, S.; Carabineiro, S.A.C.; Taj, M.B.; Bibi, I.; Raheel, A.; Javed, T.; Yahya, R.; Alelwani, W.; Verpoort, F.; Kamwilaisak, K.; et al. Green Synthesis and Photocatalytic Dye Degradation Activity of CuO Nanoparticles. *Catalysts* **2023**, *13*, 502. [CrossRef]
44. Ahsani-Namin, Z.; Norouzbeigi, R.; Shayesteh, H. Green Mediated Combustion Synthesis of Copper Zinc Oxide Using Eryngium Planum Leaf Extract as a Natural Green Fuel: Excellent Adsorption Capacity towards Congo Red Dye. *Ceram. Int.* **2022**, *48*, 20961–20973. [CrossRef]
45. Jawad, A.H.; Malek, N.N.A.; Khadiran, T.; ALOthman, Z.A.; Yaseen, Z.M. Mesoporous High-Surface-Area Activated Carbon from Biomass Waste via Microwave-Assisted-H_3PO_4 Activation for Methylene Blue Dye Adsorption: An Optimized Process. *Diam. Relat. Mater.* **2022**, *128*, 109288. [CrossRef]
46. Umar, M.; Farooq, M.U.; Arshad, M.; Usama, M.; Akbal, F.; Hussain, S.; Khan, H. Adsorptive Removal of Cationic Dyes from Wastewater Using a Novel Sodium Alginate-Based Iron Oxide Nanocomposite Hydrogel: DFT and Advanced Statistical Physics Modelling. *Process Saf. Environ. Prot.* **2024**, *190*, 85–97. [CrossRef]
47. Kamran, U.; Bhatti, H.N.; Noreen, S.; Tahir, M.A.; Park, S.-J. Chemically Modified Sugarcane Bagasse-Based Biocomposites for Efficient Removal of Acid Red 1 Dye: Kinetics, Isotherms, Thermodynamics, and Desorption Studies. *Chemosphere* **2022**, *291*, 132796. [CrossRef]
48. Akter, J.; Sapkota, K.P.; Hanif, M.A.; Islam, M.A.; Abbas, H.G.; Hahn, J.R. Kinetically Controlled Selective Synthesis of Cu_2O and CuO Nanoparticles toward Enhanced Degradation of Methylene Blue Using Ultraviolet and Sun Light. *Mater. Sci. Semicond. Process.* **2021**, *123*, 105570. [CrossRef]
49. Robati, D.; Mirza, B.; Rajabi, M.; Moradi, O.; Tyagi, I.; Agarwal, S.; Gupta, V.K. Removal of Hazardous Dyes-BR 12 and Methyl Orange Using Graphene Oxide as an Adsorbent from Aqueous Phase. *Chem. Eng. J.* **2016**, *284*, 687–697. [CrossRef]
50. Azghandi, A.V.; Zakariapoornaeini, M.; Rezazadeh, N.; Ghassemi, S.A. Evaluation and Comparison of the Performance of Immobilized and Suspended UV/TiO_2 Helical Reactor in Photocatalytic Degradation of Methyl Orange. *J. Mol. Liq.* **2025**, *439*, 128940. [CrossRef]
51. Ong, S.A.; Min, O.M.; Ho, L.N.; Wong, Y.S. Comparative Study on Photocatalytic Degradation of Mono Azo Dye Acid Orange 7 and Methyl Orange under Solar Light Irradiation. *Water Air Soil Pollut.* **2012**, *223*, 5483–5493. [CrossRef]
52. Areti, H.A.; Abo, L.D.; Jabesa, A.; Jayakumar, M.; Hamda, A.S.; Negewo, D.L.; Bedasa, O.; Geleta, B.T.; Baskar, G.; Manivannan, S. Bio-Composite-Mediated Chromium (VI) Removal from Aqueous Solutions: Nonlinear Isotherms, Kinetics, and Thermodynamic Study. *Chem. Eng. J. Adv.* **2025**, *24*, 100930. [CrossRef]

53. Ansari, F.; Sheibani, S.; Fernández-García, M. Characterization and Performance of Cu_2O Nanostructures on Cu Wire Photocatalyst Synthesized In-Situ by Chemical and Thermal Oxidation. *J. Mater. Sci. Mater. Electron.* **2019**, *30*, 13675–13689. [CrossRef]
54. Weber, W.J.; Morris, J.C. Kinetics of Adsorption on Carbon from Solution. *J. Sanit. Eng. Div.* **1963**, *89*, 31–59. [CrossRef]
55. Hou, M.; He, Y.; Yang, X.; Yang, Y.; Lin, X.; Feng, Y.; Kan, H.; Hu, H.; He, X.; Liu, C. Preparation of Biomass Biochar with Components of Similar Proportions and Its Methylene Blue Adsorption. *Molecules* **2023**, *28*, 6261. [CrossRef] [PubMed]
56. Sibiya-Dlomo, N.P.; Monama, T.P.; Govender, A.; Rathilal, S. Reduction of Pb (II) and Cu (II) Ions from Synthetic Wastewater Utilizing Magnetic Adsorbent Derived from Banana Peels: Kinetic and Isotherm Analyses. *Clean. Chem. Eng.* **2025**, *12*, 100213. [CrossRef]
57. Bakhtaoui, Y.; Ben Ali, M.; Ouakki, M.; El Khattabi, O.; El Azzouzi, N.; Srhir, B. Efficient Adsorption of Methylene Blue onto Raw Olive Pomace from Moroccan Industrial Oil Mills: Linear and Nonlinear Isotherm and Kinetic Modeling with Error Analysis. *Next Mater.* **2025**, *9*, 101072. [CrossRef]
58. Li, X.; Jiang, Y.; Cheng, W.; Li, Y.; Xu, X.; Lin, K. Mesoporous TiO_2/Carbon Beads: One-Pot Preparation and Their Application in Visible-Light-Induced Photodegradation. *Nanomicro Lett.* **2015**, *7*, 243–254. [CrossRef] [PubMed]
59. Muthukrishnaraj, A.; Al-Zahrani, S.A.; Al Otaibi, A.; Kalaivani, S.S.; Manikandan, A.; Balasubramanian, N.; Bilgrami, A.L.; Ahamed, M.A.R.; Khan, A.; Asiri, A.M.; et al. Enhanced Photocatalytic Activity of Cu_2O Cabbage/RGO Nanocomposites under Visible Light Irradiation. *Polymers* **2021**, *13*, 1712. [CrossRef]

Disclaimer/Publisher's Note: The statements, opinions and data contained in all publications are solely those of the individual author(s) and contributor(s) and not of MDPI and/or the editor(s). MDPI and/or the editor(s) disclaim responsibility for any injury to people or property resulting from any ideas, methods, instructions or products referred to in the content.